Density functional calculations on the charge-ordered and valence-mixed modification of $YBaFe_2O_5$

Christian Spiel, Peter Blaha, and Karlheinz Schwarz
Department of Materials Chemistry, Vienna University of Technology, A-1060 Vienna, Austria
(Received 27 October 2008; published 23 March 2009)

Density functional theory (DFT)-based calculations for both the charge-ordered and the valence-mixed phases of $YBaFe_2O_5$ have been performed using the WIEN2K package and the generalized gradient approximation (GGA)+U method. $YBaFe_2O_5$ crystallizes in an oxygen-deficient perovskitelike structure featuring corner-sharing distorted square FeO_5 pyramids separated by a layer of yttrium atoms in the c direction. It shows antiferromagnetic ordering below the Néel temperature of 430 K, below which it can be characterized as a Robin-Day class-III mixed-valence (MV) compound in which all iron atoms have the same noninteger oxidation state of 2.5. This compound is of particular interest since it undergoes a Verwey transition at approximately 309 K. Below the Verwey temperature the existence of two independent iron sites are found experimentally, which are occupied by fully localized divalent and trivalent iron atoms. This charge-ordered modification can thus be classified as a class-I MV compound. The Verwey transition of $YBaFe_2O_5$ is a first-order phase transition between low-temperature charge-ordered and high-temperature valence-mixed modifications which is accompanied with a dramatic change in the electronic configuration of the iron ions. For both phases the electronic and magnetic structures as well as electric field gradients, isomer shifts, and hyperfine fields have been calculated and compared to the experimental data. The value of U_{eff} (needed for the GGA+U calculation) has been estimated using a constrained DFT method. Different magnetic arrangements have been calculated in order to investigate the magnetic interactions and exchange parameters J, from which it was possible to verify the experimentally observed magnetic structures for both modifications.

DOI: 10.1103/PhysRevB.79.115123 PACS number(s): 71.27.+a, 71.28.+d, 75.10.−b

I. INTRODUCTION

Electronic, magnetic, and structural phase transitions in mixed-valence (MV) transition-metal oxides are of great interest for quite some time. Various mixed-valence compounds have been studied for many decades because of their interesting and diverse properties such as high-T_c superconductivity in yttrium barium copper oxide (YBCO) or even their practical use as color pigments. Mixed-valence compounds are usually subdivided into *three* different classes, called Robin-Day[1] classes. These classes are characterized by the electronic properties of the compound. Class I describes an insulating compound showing fully charge-ordered (CO) behavior with well-localized electrons on all crystallographic positions, whereas class III stands for completely delocalized electrons. Class II is located somewhere in between as there are ions of different oxidation states but electron transfer between them may occur with only a small amount of energy. Some of the various known mixed-valence compounds show a temperature-dependent transition from one of the MV classes to another, the so-called Verwey transition.[2] The most famous and best studied example is the Verwey transition of magnetite (Fe_3O_4). It occurs at 124 K and is still a major topic of research in solid-state science[3] since its discovery in the 1930s. The biggest problem in this puzzle is the experimental difficulty to accurately solve the low-temperature and low-symmetry structure of magnetite.

In this work a similar but much simpler double-cell perovskite system, namely, $YBaFe_2O_5$, for which the structural changes are well known, has been studied by first-principles calculations using density functional theory (DFT) (Refs. 4 and 5) as implemented in the WIEN2K software package.[6] This antiferromagnetic (AFM) compound is of particular interest since the structural and magnetic transitions and the charge ordering are highly correlated and thus can be studied simultaneously. This compound has been studied experimentally by Woodward and Karen.[7] Papers by the same authors can be found in the literature on the isostructural compounds $SmBaFe_2O_5$,[8] $TbBaFe_2O_5$,[9] and $GdBaFe_2O_5$.[10]

The Verwey transition of $YBaFe_2O_5$ is actually divided into two parts; the first transition occurs at 309 K and is accompanied with a change in structure from the low-temperature CO to the high-temperature valence-mixed (VM) modification. The structure changes from a strongly distorted orthorhombic to a nearly tetragonal symmetry. Above 309 K $YBaFe_2O_5$ corresponds to a class-II MV compound with partially delocalized electrons. With this structural change the magnetic arrangement and the conducting behavior are also significantly modified. The name *valence mixed* was chosen to distinguish it from a common mixed-valence compound as both phases fall into one of the Robin-Day mixed-valence classes. Above 334 K $YBaFe_2O_5$ eventually switches to a fully class-III state where the ordered packing of divalent and trivalent iron atoms (present in the CO phase) is merged into a single iron site with a noninteger oxidation state of 2.5. This second transition can be monitored using differential scanning calorimetry but no further structural change takes place. By further increasing the temperature one eventually reaches the Néel temperature of 430 K at which the antiferromagnetic $YBaFe_2O_5$ switches to a paramagnetic behavior and tetragonal symmetry.

First-principles calculations are a well-suited tool to highlight the changes when passing through the Verwey transition. In a recent paper by Hao *et al.*[11] the electronic structure

TABLE I. Atomic sphere radii R_{MT} (in bohr and Å) used in the calculations.

	R_{MT}	
Atom	bohr	Å
Ba	2.48	1.31
Y	2.26	1.20
Fe	1.79	0.95
O	1.59	0.84

of the CO phase was already studied, whereas in the present work we also investigated the changes in the electronic and magnetic structures for both the CO and VM modifications as well as for several other different magnetic phases and their corresponding geometric structures. This allows the determination of exchange parameters. Furthermore we calculated electric field gradients (EFGs), isomer shifts, and hyperfine fields for both modifications and compared the results with Mössbauer experiments, which are very well suited to check the quality of the calculations.

II. COMPUTATIONAL DETAILS

All calculations were performed with the WIEN2K software package.[6] This DFT-based software implements the full-potential augmented plane wave (APW)+lo/linearized augmented plane wave (LAPW)+local orbital (LO) method and offers the possibility to explore different exchange-correlation potentials.[12] The plane-wave cutoff, defined by the product of the smallest atomic sphere radius times the magnitude of the largest reciprocal-lattice vector $R_{MT_{\min}}K_{\max}$, was set to 7.0 and a $G_{\max}$ (magnitude of the largest vector in the charge-density Fourier expansion) of 12 was used for all calculations. 328 (CO) and 656 (VM) LOs were added for the description of lower-lying *s*, *p*, and *d* semicore states. The atomic sphere radii used in all calculations are listed in Table I. They were kept constant for both modifications in order to be able to compare the results of the CO and VM phases. The number of *k* points in the whole Brillouin zone was set to 100 for the CO phase and 50 for the VM phase (whose supercell is twice as large), resulting in 8 (CO) and 4 (VM) *k* points in the irreducible Brillouin zone, respectively. Spin-orbit coupling was considered in all the calculations in a second variational procedure.

We used both the local spin-density approximation (LSDA) (Ref. 13) and the generalized gradient approximation (GGA) due to Perdew *et al.*[14] to describe exchange and correlation. Since it is well known that such calculations cannot describe the strong on-site correlation between the Fe *d* electrons, we added an effective Coulomb interaction $U_{\text{eff}}=U-J$ for them. These rotationally invariant GGA+*U* calculations (with the standard double-counting correction[15]) were performed under variation in the U_{eff} value. In a free atom U_{eff} would correspond to F^0 of the unscreened Slater integrals,[16] but in a solid F^0 is partially screened. The value of U_{eff} generally increases with ionicity and with the contraction of the *d*-wave function across the 3*d* transition-metal series.[17] U_{eff} can be estimated by constraint DFT calculations, where some of the valence electrons are selectively treated as core electrons to switch off any hybridization with other electrons.[16] One can artificially simulate the addition and removal of electrons to the atomic shell and observe the change in the calculated total energy in order to estimate U_{eff}. We used the AFM supercells for such calculations and assumed a high-spin configuration for the d^6 and d^5 Fe ions, respectively. This assumption is supported by the data from neutron powder diffraction (NPD) measurements.[7] For these constrained calculations the symmetry of the system was lowered in order to allow the originally equivalent iron atoms to be treated individually. One divalent and one trivalent iron sites were selected independently for each estimation. Adding and removing electrons were achieved by explicitly modifying the *d*-occupation numbers for these iron atoms. From the total energy corresponding to individual electronic configurations U_{eff} can be estimated using the following equation (which also corrects for the change in Fermi energy ε_F):

$$F_0^{\text{eff}} = \varepsilon_{3d\uparrow}\left(+\frac{1}{2}e\right) - \varepsilon_{3d\uparrow}\left(-\frac{1}{2}e\right) - \varepsilon_F\left(+\frac{1}{2}e\right) + \varepsilon_F\left(-\frac{1}{2}e\right), \tag{1}$$

where $\varepsilon_{3d\uparrow}$ stands for the 3*d* spin-up eigenvalue of the iron atom. The results of this estimation are listed in Table II and fall within the expected range of 6–8 eV. These values are close to the results of Madsen and Novák[17] for magnetite. Thus we used a value of 7 eV for U_{eff} for all our calculations (unless stated explicitly) since such an estimation usually carries an error of ~20%. In order to determine how some of the results depend on U_{eff}, we varied U_{eff} between 5 and 8 eV in steps of 1 eV and monitor the dependence of these results.

TABLE II. Estimation of U_{eff} (in eV) for the different Fe sites in the CO and VM phases.

Phase	CO		VM
Ion	$Fe1^{3+}$	$Fe2^{2+}$	$Fe^{2.5+}$
U_{eff}	7.52	7.22	6.58

III. STRUCTURE

A. Crystallographic structures

Both investigated modifications of $YBaFe_2O_5$ (CO and VM) crystallize as orthorhombic double-cell perovskites according to NPD measurements.[7] In Table III the structural parameters of both phases are given. The CO phase can be refined in the *Pmma* space group whereas the VM phase was found to be in the higher-symmetry *Pmmm* space group. The ordering of the iron cations and the oxygen vacancies in the different layers is stabilized by the different size of the Y^{3+} and Ba^{2+} ions, respectively. The fact that the iron atoms are separated by an yttrium layer in the *z* direction leads to an

TABLE III. Crystallographic data of the CO and VM phase of $YBaFe_2O_5$ (Ref. 7). Lattice parameters are given in Å and volume in Å^3. Theoretical atomic positions are optimized within GGA+U, U_{eff}=7 eV.

Unit-cell parameters		
Phase	CO	VM
Temperature	<309 K	>309 K
Space group	*Pmma* (51)	*Pmmm* (47)
a	8.02507	3.93182
b	3.83834	3.91718
c	7.53122	7.56826
Volume	231.984	116.564

Atomic positions

		Measured (Ref. 7)			Theory				Measured (Ref. 7)			Theory		
Atom	Wyckoff	*x*	*y*	*z*	*x*	*y*	*z*	Wyckoff	*x*	*y*	*z*	*x*	*y*	*z*
Ba	2*a*	0	0	0	0	0	0	1*a*	0	0	0	0	0	0
Y	2*c*	0	0	$\frac{1}{2}$	0	0	$\frac{1}{2}$	1*c*	0	0	$\frac{1}{2}$	0	0	$\frac{1}{2}$
$Fe1^{3+}$	2*f*	$\frac{1}{4}$	$\frac{1}{2}$	0.2542	$\frac{1}{4}$	$\frac{1}{2}$	0.2557							
$Fe2^{2+}$	2*f*	$\frac{3}{4}$	$\frac{1}{2}$	0.2695	$\frac{3}{4}$	$\frac{1}{2}$	0.2695	2*t*	$\frac{1}{2}$	$\frac{1}{2}$	0.2641	$\frac{1}{2}$	$\frac{1}{2}$	0.2718
O1	2*f*	$\frac{1}{4}$	$\frac{1}{2}$	0.0030	$\frac{1}{4}$	$\frac{1}{2}$	0.0035	1*f*	$\frac{1}{2}$	$\frac{1}{2}$	0	$\frac{1}{2}$	$\frac{1}{2}$	0
O 2*a*	2*e*	$\frac{3}{4}$	0	0.3213	$\frac{3}{4}$	0	0.3257							
O 2*b*	2*e*	$\frac{1}{4}$	0	0.3132	$\frac{1}{4}$	0	0.3138	2*s*	$\frac{1}{2}$	0	0.3140	$\frac{1}{2}$	0	0.3125
O3	4*j*	0.0098	$\frac{1}{2}$	0.3119	0.0121	$\frac{1}{2}$	0.3129	2*r*	0	$\frac{1}{2}$	0.3125	0	$\frac{1}{2}$	0.3117

unusual coordination of iron by the oxygen ligands, namely, a distorted square pyramid, whereas a fivefold coordinated ion would usually prefer a trigonal-bipyramidal coordination. For stoichiometric $YBaFe_2O_5$ a noninteger formal oxidation state of 2.5 is deduced for the iron atoms. For the CO modification this noninteger valence is split into two crystallographic sites with divalent and trivalent iron ions, whereas for the VM modification only one crystallographic iron site has been found experimentally, thus preserving the unusual noninteger valence on all equivalent iron sites. For the CO phase the iron ions of the same oxidation state arrange in *chains* along the *b* direction, in contradiction to the Anderson charge-ordering condition,[18] which would favor minimal electrostatic repulsion and thus would lead to a checkerboardlike pattern of the different oxidation states. This electrostatic instability has to be compensated by a certain magnetic/orbital ordering in the CO phase which implies a strong electron-lattice coupling and a distortion of the structure. The bond lengths between the iron and the oxygen atoms of both structures are listed in Table IV. The different bond lengths suggest the d_{xz} orbital as a possible candidate for orbital ordering as can also be seen from the ratio of the lattice constants. To check the stability of this distortion we optimized the internal position parameters with GGA+U calculations but using the experimental lattice parameters. The results are given in Table III and will be discussed below. We used these optimized structures for all further calculations.

The CO modification shows a significant orthorhombic distortion in the *xz* plane both in the experimental and in the optimized structures, which agree well. There are three different Fe-O bond lengths in the *x*, *y*, and *z* directions, respectively. The divalent $Fe2^{2+}$ ion has the shortest Fe-O bond in the *y* direction (1.96 Å), while the bonds in the *z* and *x* directions are 0.09 and 0.16 Å longer, respectively. On the other hand, the trivalent $Fe1^{3+}$ ion has a much shorter Fe-O bond in the *z* direction (1.899 Å), whereas the bonds in both the *x* and *y* directions are only 0.06 Å longer. It should be mentioned that an optimization with GGA leads to a metallic phase (see below), virtually no charge order and thus to fairly similar $Fe1^{3+}$-O1 and $Fe2^{2+}$-O1 distances of 1.96 and 1.99 Å, respectively, in strong contrast to the experimental or GGA+U results.

The experimental VM phase is only marginally distorted and thus adopts a nearly tetragonal symmetry. This changes somewhat with the optimization of the internal parameters where the VM modification gets distorted in the *z* direction (with a change in bond length of Fe to O1 from 1.999 to

TABLE IV. Experimental (Ref. 7) and theoretical [within GGA+U (U_{eff}=7 eV)] iron-oxygen and Fe-Fe bond lengths (in Å).

Bond	Direction	CO		VM	
		Expt.	Theor.	Expt.	Theor.
$Fe1^{3+}$-O1	*z*	1.892	1.899	1.999	2.056
$Fe2^{2+}$-O1		2.052	2.057		
$Fe1^{3+}$-O2*b*	*y*	1.970	1.968	1.995	1.983
$Fe2^{2+}$-O2*a*		1.958	1.965		
$Fe1^{3+}$-O3	*x*	1.976	1.957	2.000	1.989
$Fe2^{2+}$-O3		2.109	2.128		
$Fe1^{3+}$-$Fe2^{2+}$	*z*	3.587	3.576	3.571	3.456

2.056 Å), while the bond lengths between Fe and O2 and O3 do not change as much. Consequently the Fe-Fe distance across the Y layer gets significantly reduced by 0.12 Å, compared to the experimental distance. These differences could be a finite temperature effect (theory calculates a static $T=0$ K structure) evidenced by the fact that above the Néel temperature (430 K), paramagnetic $YBaFe_2O_5$ eventually adopts a tetragonal symmetry with space group $P4/mmm$.[7]

The CO phase consists of distorted square pyramids of FeO_5 units which are corner shared. The direction and size of this distortion are cooperative throughout the crystal. The driving force behind it is the preferential occupation of the lower-energy d orbitals. Although in this case the iron d orbitals are not truly degenerate, one can use the term *cooperative Jahn-Teller distortion* (CJTD) for this phenomenon as defined by Goodenough.[19] Nowadays the term *orbital ordering* is often used to describe the same effect. The structural change in $YBaFe_2O_5$ at the Verwey temperature can therefore be mainly attributed to the change in charge order which of course also modifies the occupation of the d orbitals (as will be shown in Sec. IV C).

B. Magnetic structures

Both modifications show AFM behavior which cannot be simulated with the crystallographic unit cell described above. Therefore larger superstructures had to be used to account for the magnetic structure. NPD measurements[7] have shown that the CO modification adopts a Wollan-Koehler type-G AFM arrangement[20] of the magnetic moments. In this antiferromagnetic arrangement each Fe atom is surrounded by nearest-neighbor irons with opposite moments in all spatial directions. All magnetic moments point in the y direction.

In the same NPD study the VM modification was refined to a different magnetic order; it showed an atypical *ferromagnetic (FM) coupling* through the Y layer which implies a somewhat surprising change in the AFM structure upon passing through the Verwey transition. The refined order of the VM phase is similar to the magnetic structure of orthorhombic $TbBaFe_2O_5$ (Ref. 9) and tetragonal AF1-type $YBaCuFeO_5$.[21] To further investigate this surprising change in magnetic order, we studied the stability of this particular setting by calculations and will discuss the results in Sec. IV E. The NPD measurements of the VM phase also showed a slight canting of the magnetic moments with respect to the z axis. This canting, however, was not considered in the present calculations and a collinear average was assumed.

Based on the NPD measurements a $1\times2\times1$ supercell of the crystallographic unit cell is necessary for calculating the CO phase, while for the VM phase with its unusual magnetic setting an even larger $2\times2\times2$ supercell had to be constructed to account for the AFM behavior (Figs. 1 and 2). The resulting supercells had four (CO) and eight (VM) independent iron sites, respectively, each with a multiplicity of 2. Based on this we use the following naming convention for the CO phase which depicts the inheritance of each iron atom. Fe1 and Fe2 refer to the Fe^{3+} and Fe^{2+} sites, respectively, and this is indicated by the color of the pyramids in Fig. 1. Due to the antiferromagnetism (indicated by the arrows in Fig. 1) the crystallographic Fe1 site becomes $Fe1_1$ and $Fe1_2$ in the CO supercell (Fe2 becomes $Fe2_1$ and $Fe2_2$). In Sec. IV E we will discuss the relative stability of different magnetic arrangements. For this purpose we had to introduce symmetry-breaking spin flips and this splits the iron sites further. Then the resulting iron positions were named in a way so that $Fe1_1$ eventually becomes $Fe1_{1\alpha}$ and $Fe1_{1\beta}$, $Fe1_2$ becomes $Fe1_{2\alpha}$ and $Fe1_{2\beta}$, and so on. The symmetry was preserved on all other atomic positions to reduce computation time. Pictures of both supercells which also show the

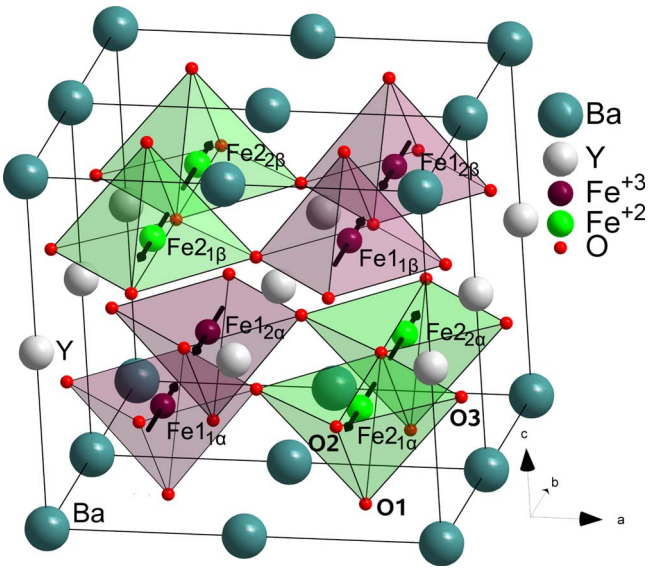

FIG. 1. (Color online) The magnetic $1\times2\times1$ CO supercell. The arrows depict the direction of the magnetic moments.

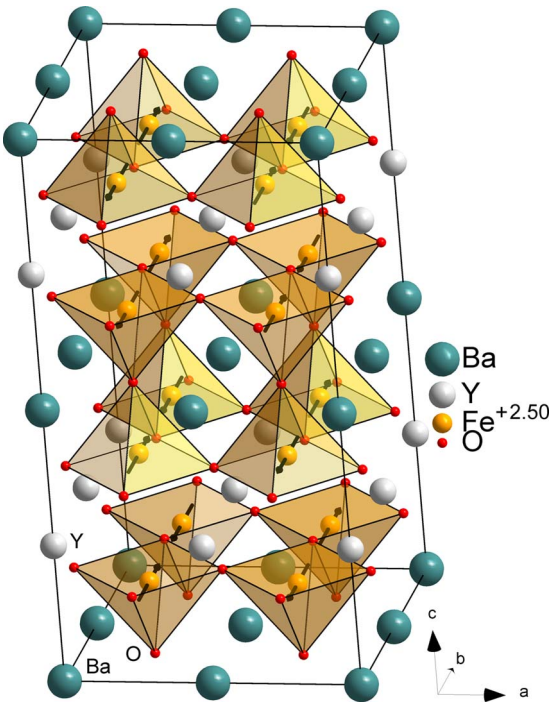

FIG. 2. (Color online) The magnetic $2\times2\times2$ VM supercell. The arrows depict the direction of the magnetic moments.

TABLE V. Dependence of the band gap (in eV), the orbital μ_{orb}, spin μ_S, and total moments μ_{tot} (in μ_B) on U_{eff} for the CO and VM phases. Experimental values are taken from Ref. 7.

	CO					VM				
	Expt.	U_{eff} (eV)				Expt.	U_{eff} (eV)			
		5	6	7	8		5	6	7	8
$\mu_{orb}Fe1^{3+}$		0.01	0.01	0.01	0.01		0.05	0.05	0.04	0.04
$\mu_{orb}Fe2^{2+}$		0.10	0.10	0.12	0.11					
$\mu_S Fe1^{3+}$		3.95	4.02	4.07	4.14		3.81	3.87	3.92	3.97
$\mu_S Fe2^{2+}$		3.34	3.38	3.42	3.45					
$\mu_{tot}Fe1^{3+}$	4.15	3.96	4.03	4.08	4.14	3.90[a]	3.86	3.91	3.96	4.01
$\mu_{tot}Fe2^{2+}$	3.65	3.44	3.49	3.54	3.56					
Band gap		1.8	2.1	2.4	2.7		0.9	1.0	1.0	1.1

[a]Extrapolated from the experimental data (Ref. 9).

arrangements of the magnetic moments can be seen in Figs. 1 and 2.

IV. RESULTS OF THE CALCULATIONS

A. General properties

$YBaFe_2O_5$ is an insulator in its low-temperature CO modification but a semiconductor in its high-temperature VM form with an specific electrical resistivity comparable to germanium (ρ_{Ge}=46 Ω cm) as measurements on the isostructural compound $TbBaFe_2O_5$ have shown.[9] This behavior can be described satisfactorily only by the GGA+U method.[15] This method is particularly well suited to describe strongly correlated transition-metal oxides such as the investigated compound. The usage of standard GGA functionals leads to metallic behavior and magnetic moments which vastly differ from the experimental values. Furthermore no charge ordering (difference in charge in the atomic spheres of the iron atoms) was found with GGA only.

However, by using the GGA+U method (with U_{eff} =7 eV as described in Sec. II), we found an insulating behavior for both structures with band gaps of ~2 (CO) and ~1 eV (VM), respectively. This agrees with the experimentally observed increase in conductivity above the Verwey transition.[22] The calculated total magnetic moments of 4.08 and 3.54μ_B for $Fe1^{3+}$ and $Fe2^{2+}$ of the CO phase and 3.96μ_B for the VM phase were also found to be in good agreement with the experiment as can be seen from Table V [for the VM modification the magnetic moments were fitted to a Brillouin-type parametric curve for $TbBaFe_2O_5$ (Ref. 9) to extrapolate their value to 0 K]. Fe can have not only a spin but also an orbital moment. As expected the orbital moment is particularly small for $Fe1^{3+}$, but also for the $Fe2^{2+}$ site the orbital moment is only 0.12μ_B. This seems to be consistent with more recent determinations in magnetite,[23] whereas a previous experiment[24] had reported a significantly larger value of 0.33μ_B. In Table V we show the dependence of magnetic moments and band gaps on the value of U_{eff}. A weak dependence was found for most results; only the band gap of the CO modification was more sensitive to the U_{eff}. As expected a larger U_{eff} slightly increases the magnetic moments of all iron atoms but also the band gap.

Using GGA+U we also obtained a lower total energy per f.u. for CO with respect to the VM phase (see Sec. IV E), making CO the more stable modification at 0 K in agreement with experiment. However, with GGA the VM phase had the lower total energy and thus would not lead to any charge order or related distortions.

B. Charge order

When studying charge order using theoretical methods one always faces the problem of defining an atomic charge in a solid, i.e., a consistent decomposition of the total charge into atomic charges. In APW-based methods this is often done by using the integrated charges within the atomic spheres which are easy to calculate. This has the disadvantage that the obtained results depend on the choice of the sphere radii R_{MT} and furthermore the interstitial charge cannot be partitioned at all using this method. However, the trends are reliable provided that one keeps the size of the spheres constant among sets of calculations. In the CO modification a significant difference in sphere charge of $0.2e^-$ between the two types of iron atoms was obtained, which strongly suggests the presence of charge ordering whereas no charge difference was observed in the VM modification.

Although we used a constant set of R_{MT} values (Table I) for all calculations in the present study, we rather decided to compare the charges obtained by a calculation based on the *atoms in molecules* (AIM) (Ref. 25) method. This scheme characterizes the chemical bonding of a system by analyzing the topology of the charge density. It divides the space into atomic volumes (basins) containing exactly one nucleus. The definition of these atomic basins is based on an interatomic surface, which satisfies the zero-flux boundary condition

$$\nabla\rho(\mathbf{r_S})\mathbf{n}(\mathbf{r_S}) = 0, \tag{2}$$

where $\mathbf{n}$ is the unit vector normal to the surface and $\nabla\rho(\mathbf{r_S})$ is the gradient of the electron density at $\mathbf{r_s}$. This decomposition is uniquely defined and thus considerably improves transferability.

Using the AIM method it is usually possible to obtain charges closer to the formal valences than by simply inte-

TABLE VI. Atomic charges obtained with AIM using U_{eff} =7 eV.

	CO		VM	
Atom	Multiplicity	Charge	Multiplicity	Charge
Ba	4	+1.51	8	+1.52
Y	4	+2.17	8	+2.15
$Fe1^{3+}$	4	+1.84	16	+1.62
$Fe2^{2+}$	4	+1.36		
O1	4	−1.36	8	−1.36
O 2*a*	4	−1.40	16	−1.39
O 2*b*	4	−1.36		
O3	8	−1.38	16	−1.39

grating the charge inside the individual atomic spheres. This was also found by our calculations (the AIM charges are listed in Table VI). The resulting charge difference of $\sim 0.5e^-$ ($Fe2^{2+}$: +1.36 vs $Fe1^{3+}$: +1.84) between the two types of iron atoms is much larger than that obtained by only comparing the sphere charges ($\sim 0.2e^-$). The charges are still much smaller than the formal valences, a fact that is typical for theoretical calculations, which always find some covalent contribution to the chemical bond. Nevertheless the size of the charge difference is a strong indication for the presence of charge order in the CO phase. One should note that for the classical charge-order system magnetite (Fe_3O_4), a similar charge transfer of about 0.2 to 0.3 e^- was found[17] within a much larger atomic sphere of 2.0 bohr. For the VM phase the charge of all iron atoms lies nicely in between the divalent and trivalent states (+1.62), supporting the presence of a fully mixed-valence state. The negative charges on the oxygen ions of about $-1.4e^-$ remain fairly constant during the Verwey transition as do the charges on Ba and Y.

C. Analysis of changes during the Verwey transition

The distribution of the electrons on the different *d* orbitals is of particular interest for understanding the distorted coordination geometry of divalent iron in the CO modification. We start out with a high-spin configuration of Fe^{2+} ions in an approximate octahedral field, i.e., one spin channel is fully occupied and the remaining electron has to occupy one of the t_{2g} orbitals. To explain the orthorhombic distortion in the *xz* plane of the unit cell, one can think of a quasi-Jahn-Teller-type distortion in the square-pyramidal ligand field. Extended Hückel calculations[7] compared the effects of a square-pyramidal coordination to the standard octahedral ligand field. The obtained results showed that for this geometry the octahedral field still dominates and the three d_{xy}, d_{xz}, and d_{yz} orbitals remain nearly degenerate in energy while the d_{z^2} orbital lies higher in energy and the $d_{x^2-y^2}$ is situated even higher. This result can be described by a simple two-step process; first an octahedral splitting (separating t_{2g} and e_g orbitals) takes place and then due to the missing second apical ligand, an additional splitting of the e_g orbitals follows. In charge-ordered $YBaFe_2O_5$ only one of the three nearly degenerate lower 3*d* orbitals has to be doubly occupied for the divalent iron ions if a high-spin configuration is assumed. Due to symmetry (because of the chainlike arrangement of the iron atoms in the *y* direction), the d_{xy} and d_{yz} orbitals can be ruled out and thus a structural stabilization (via a second-order Jahn-Teller distortion) can only occur if the d_{xz} orbital is doubly occupied. This leads to the observed expansion of two out of four Fe^{2+}-O bonds in the basal plane of the square pyramid (see Table IV) which corresponds to the distortion of the iron-oxygen bond lengths in the *x* and *z* directions of the unit cell. The partial charges (inside the corresponding spheres) for the individual *d* orbitals of all iron atoms and with respect to the spin direction are given in Table VII for both the CO and VM modifications. One can easily verify that the electronic distribution for the CO, $YBaFe_2O_5$ is in fact as expected from the simple crystal-field arguments described above. The obtained $Fe2^{2+}$-d_{xz} partial charges of 0.86 and $0.83e^-$ for spin-up and spin-down contributions correspond to a nearly fully occupied orbital whereas all other *d* orbitals show no significant spin-down contribution. Therefore the observed distortion goes hand in hand with the stabilization of the d_{xz} orbital.

TABLE VII. Partial 3*d* charges inside the corresponding spheres (per spin) for the $Fe2^{2+}$ and $Fe1^{3+}$ (CO) and $Fe^{2.5+}$ (VM) *d* orbitals of the iron atoms. Results are for U_{eff}=7 eV.

Phase	Ion	Spin	d_{z^2}	$d_{x^2-y^2}$	d_{xy}	d_{xz}	d_{yz}
CO	$Fe2^{2+}$	Up	0.866	0.908	0.884	0.859	0.884
		Down	0.040	0.068	0.020	0.829	0.028
	$Fe1^{3+}$	Up	0.908	0.933	0.908	0.908	0.907
		Down	0.132	0.168	0.045	0.077	0.069
VM	$Fe^{2.5+}$	Up	0.916	0.945	0.921	0.918	0.918
		Down	0.390	0.138	0.039	0.041	0.040

The trivalent iron $Fe1^{3+}$ has a formal occupation of five spin-up electrons only. Consequently the d_{xz} spin-down orbital is empty. We find additional contributions of $\sim 0.3e^-$ in the spin-down e_g-like d_{z^2} and $d_{x^2-y^2}$ orbitals due to covalency effects with oxygen. The small difference in occupation can be attributed to the different geometric environment of the trivalent iron ions; on one hand the bond lengths in the *x* and *y* directions are longer than in the *z* axis, on the other hand there is only one ligand in the *z* direction. Apparently the present geometry favors the $d_{x^2-y^2}$ orbital a tiny bit more than the d_{z^2}.

For the VM phase with its formal occupation of $5.5e^-$ a similar distribution pattern is obtained, but the d_{z^2} orbital is clearly favored over $d_{x^2-y^2}$; according to the density of states (DOS)—discussed in the next paragraph—the d_{z^2} orbital is situated at the top of the valence band with a formal occupation of $\sim$0.9 (spin up) and $\sim$0.4 electrons (spin down), while the $d_{x^2-y^2}$ orbital shows a significant spin-down contribution of $0.14e^-$. Both spin-down charges sum up to approximately half an electron.

The total DOS and the Fe and O contribution (projected within their atomic spheres) for both modifications are shown in Fig. 3 using the GGA approach and in Fig. 4 for

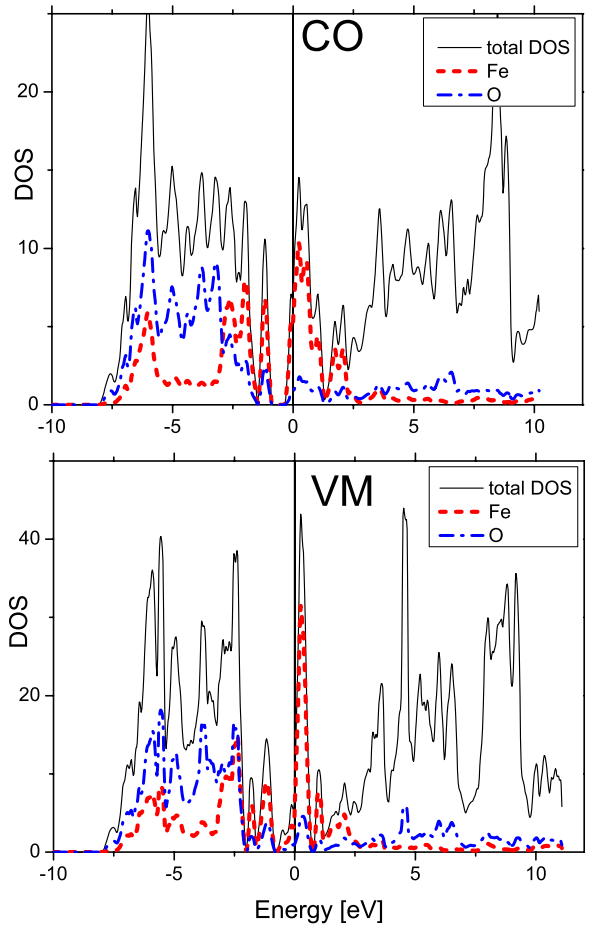

FIG. 3. (Color online) Total density of states (black full lines), Fe (red dashes), and O (blue dashed dotted) contributions (projected inside their atomic spheres) to the DOS using GGA (in states/eV/cell). Top figure shows CO; bottom figure shows VM modification.

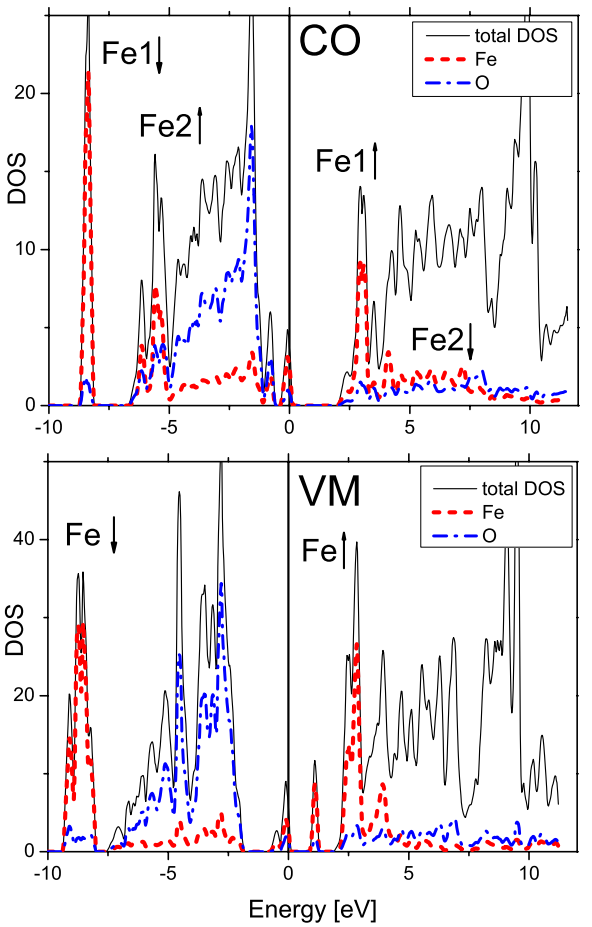

FIG. 4. (Color online) Total density of states (black full lines), Fe (red dashes), and O (blue dashed dotted) contributions (projected inside their atomic spheres) to the DOS using GGA+U (U_{eff}=7 eV) (in states/eV/cell). Top figure shows CO; bottom figure shows VM modification. The contributions from different Fe atoms are also indicated

GGA+U, highlighting the changes when passing through the Verwey transition from the CO (top) to the VM (bottom) phase. Lower-lying states (below −10 eV, not shown in Figs. 3 and 4) originate from O 2s and spin-orbit split Ba 5p states.

Let us first discuss the GGA DOS (Fig. 3). A broad band from −8 to −1.5 eV followed by a narrow peak around −1.2 eV originates from the majority-spin states. These bands have predominantly O 2p character, but at the bottom of the broad band and in the narrow peak bonding/antibonding Fe-e_g contributions are evident, while the nonbonding Fe-t_{2g} states dominate at the top of the broad band. A small gap below ε_F separates spin-up and down states, but a metallic character is evident since the Fe spin-down states are not split around ε_F. As expected the differences in the DOS between CO and VM phases are rather small since GGA does not lead to charge order.

On the other hand in GGA+U calculations (Fig. 4) a lower Hubbard band around −8 eV splits off and both modifications are insulating with an interesting splitting of the VM DOS into two small peaks around ε_F. The single lower Hubbard band of the VM phase splits in the CO phase into peaks originating from spin-up $Fe1^{3+}$ (around −8.5 eV) and spin-down $Fe2^{2+}$ (around −6.5 eV). The corresponding states with opposite spin are about 10 eV higher in energy and unoccupied. For further analysis we calculated the partial d DOS decomposed into the individual orbitals to investigate its bonding/antibonding behavior. The results are shown in Figs. 5–7 for both structures. For $Fe2^{2+}$ in the CO phase (Fig. 5) we find rather localized peaks for four out of the five spin-up orbitals with an additional characteristic bonding/antibonding splitting of the e_g-like states. The d_{xz} states are rather delocalized over the whole O p band indicating some weak Fe-O π interaction. On the other hand for this d_{xz} orbital also spin down is occupied forming a localized peak just below ε_F, while the other 3d spin-down orbitals are quite delocalized and at much higher energies. For obvious electrostatic reasons the very localized spin-down d states of $Fe1^{3+}$ (Fig. 6) are all lower in energy than the $Fe2^{2+}$ states and also the unoccupied orbitals show a fairly localized nature. Also in the VM modification (Fig. 7) the occupied Fe states are fairly low in energy and well localized. The partly occupied spin-up d_{z^2} states split up into two peaks around ε_F, forming a bonding/antibonding gap and leading to

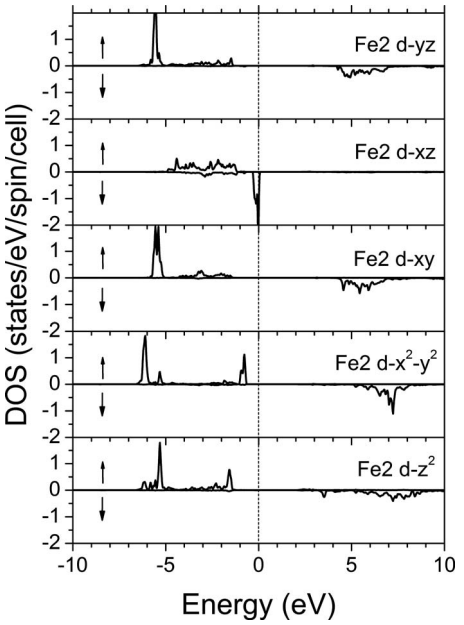

FIG. 5. Partial d DOS (projected inside the Fe spheres) of $Fe2^{2+}$ ions in the CO state (GGA+U with U_{eff}=7 eV). Arrows indicate spin and ε_F is set to 0 eV.

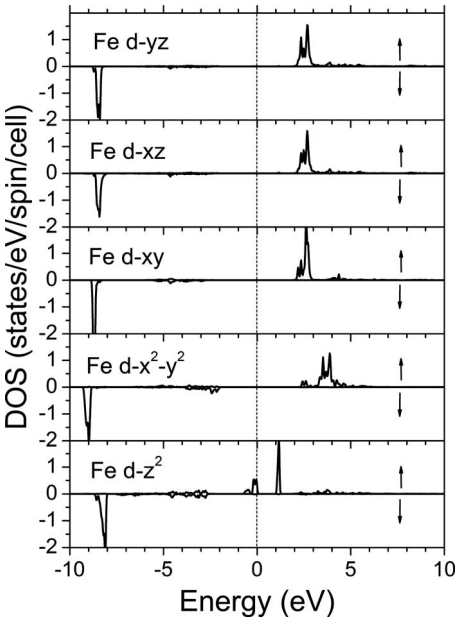

FIG. 7. Partial d DOS (projected inside the Fe spheres) of the d orbitals of $Fe^{2.5+}$ ions in the VM state (GGA+U with U_{eff}=7 eV). Arrows indicate spin and ε_F is set to 0 eV.

the two peaks (one occupied and one empty) mentioned above.

In order to make the differences between the CO and VM phases even more clear, we show the difference electron densities ($\delta\rho=\rho_{\mathrm{crystal}}-\rho_{\mathrm{atoms}}^{\mathrm{superposition}}$) in Figs. 8 and 9. Most noticeable are the changes around the Fe sites. In the CO phase the occupied spin-down d_{xz} orbital on $Fe2^{2+}$ is clearly visible, while for $Fe1^{3+}$ a fairly spherical negative $\delta\rho$ can be seen. On the other hand for the VM phase the d_{z^2} orbital dominates, in agreement with the partial charge analysis given in Table VII. This could be interpreted as strong covalent Fe-O1 σ bond but also as direct Fe-Fe interaction across the Y layer. The latter may also explain the difference in the magnetic structure between the two phases. The overall charge transfer toward oxygen manifests itself in a positive $\delta\rho$ around oxygen. Although oxygen has formally a full $2p$ shell, a significant anisotropy can be seen. In particular on the O1 site some p_z charge is missing since antibonding Fe-O1 states are pushed above ε_F. Nevertheless, the polarization of O1 by electrostatic interactions is even stronger, since we find in the CO phase a charge accumulation toward $Fe1^{3+}$ (the short Fe-O1 bond), but a depletion toward $Fe2^{2+}$ (with the longer bond). Such a polarization is also present on the O3 sites with charge accumulation toward the $Fe1^{3+}$ site.

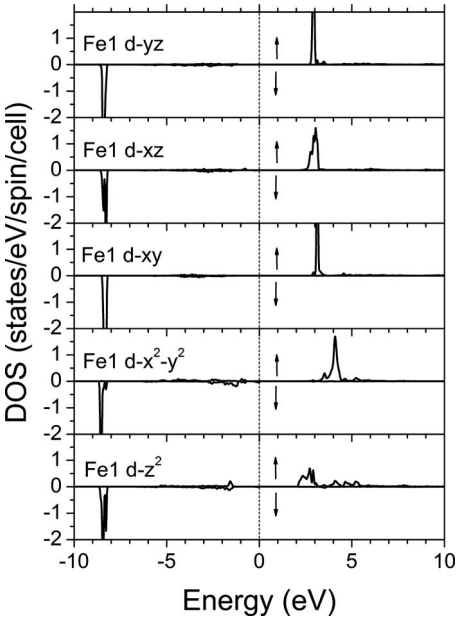

FIG. 6. Partial d DOS (projected inside the Fe spheres) of $Fe1^{3+}$ ions in the CO state (GGA+U with U_{eff}=7 eV). Arrows indicate spin and ε_F is set to 0 eV.

D. Calculation of Mössbauer parameters

For the two investigated phases the hyperfine fields, isomer shifts, electric field gradients (EFGs) and the closely related quadrupole splittings at the Fe sites were calculated and compared to the experimental values. These parameters are very sensitive to even small changes in the electronic structure of the ions and thus are well suited to test the quality of our theoretical results. The calculations were done—as for the magnetic moments—for a series of U_{eff} values (using atomic positions optimized with U_{eff}=7 eV) and also in LDA and GGA (using the experimental positions) to evaluate how sensitive these quantities are on the treatment of exchange and correlation. In addition we mention that the different atomic positions have a fairly modest influence on most quantities. The only significant change occurs for the EFG, i.e., the eQV_{zz} value of the VM phase, which is around −1.0 mm/s in GGA+U calculations in disagreement with

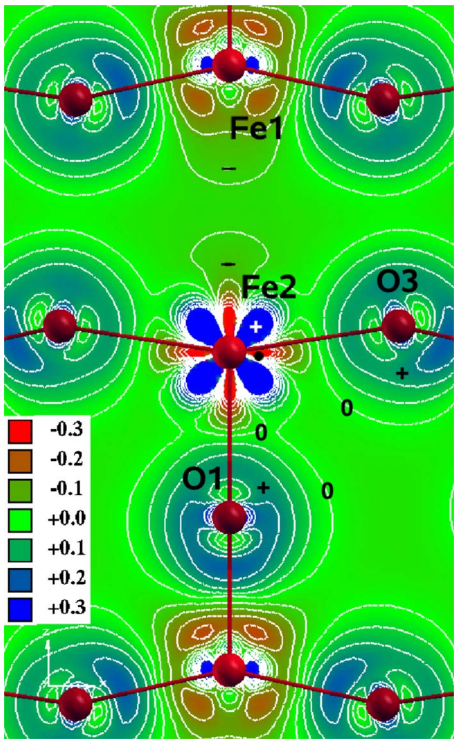

FIG. 8. (Color online) Difference density of the CO phase in the (020) plane. [graph produced using XCRYSDEN (Ref. 26); contour lines differ by $0.05e/\text{Å}^3$].

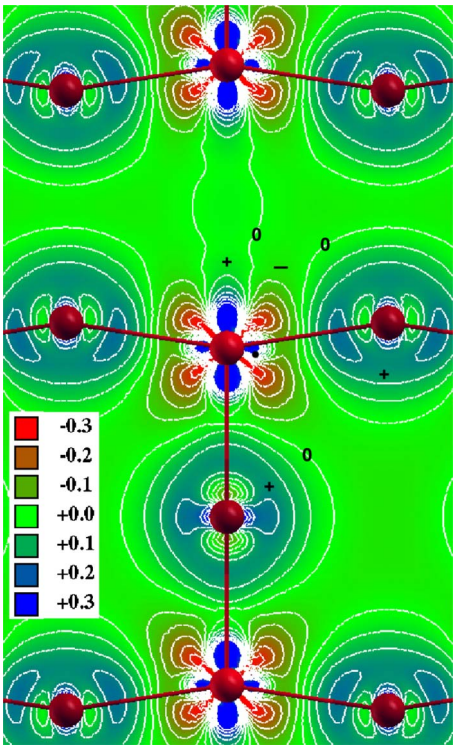

FIG. 9. (Color online) Difference density of the VM phase in the (020) plane. Details analogous to Fig. 8.

experiment. The experimental values were taken from Mössbauer experiments on $GdBaFe_2O_5$,[10] $TbBaFe_2O_5$,[9] and $SmBaFe_2O_5$,[8] respectively. The results are listed in Table VIII for the CO phase and in Table IX for the VM phase. The contributions to the total hyperfine field B_{tot} listed in the table are the Fermi contact term $B_{contact}$, the dipolar field B_{dip}, and the field associated with the orbital moment B_{orb}. In general the results are in good agreement with the experiments.

Of particular interest is the rather large contribution of the orbital and spin-dipolar parts to the hyperfine fields for divalent iron in the CO phase as compared to the trivalent species, although the corresponding orbital moments μ_{orb} are only $\sim 0.1\mu_B$. Only the GGA+U results agree with experiment and the difference to the GGA or LSDA results stems primarily from the different dipolar ($\sim$17 vs $\sim$13 T for GGA) and orbital contributions ($\sim$7.5 vs $\sim$6 T). The hyperfine field of trivalent iron is dominated by the contact term $B_{contact}$, for which GGA+U gives significantly larger values than GGA, but in total it is underestimated, a fact that is not uncommon for DFT-based calculations. For the VM com-

TABLE VIII. Hyperfine fields B (in T), isomer shifts δ (mm/s), and quadrupole coupling constants eQV_{zz} (mm/s) for the CO phase for various exchange and correlation potentials and experiment (Refs. 8–10).

		Expt.	GGA+U				LDA	GGA
	U_{eff} (eV)		5	6	7	8		
$Fe2^{2+}$	B_{dip}		−16.29	−16.49	−16.66	−16.83	−6.68	−12.67
	B_{orb}		−6.73	−6.90	−8.26	−7.65	−9.57	−6.34
	$B_{contact}$		32.25	32.23	32.58	32.60	32.21	31.58
	B_{tot}	∼8	9.23	8.83	7.66	8.13	15.96	12.57
	δ	∼1	0.92	0.94	0.96	0.99	0.74	0.79
	eQV_{zz}	3.6–4[a]	3.66	3.74	3.81	3.89	−0.82	2.60
$Fe1^{3+}$	B_{dip}		−0.67	−0.60	−0.52	−0.45	1.29	0.39
	B_{orb}		−0.52	−0.45	−0.37	−0.28	−7.96	−2.65
	$B_{contact}$		37.65	38.28	38.15	37.86	29.64	31.63
	B_{tot}	∼50	36.46	37.24	37.26	37.12	22.97	29.37
	δ	∼0.4	0.33	0.30	0.28	0.25	0.50	0.47
	eQV_{zz}	1–1.5[a]	1.46	1.50	1.51	1.52	1.04	−0.30

[a]Depending on rare-earth ion.

TABLE IX. Hyperfine fields B (in T), isomer shifts δ (mm/s), and quadrupole coupling constants eQV_{zz} (mm/s) for the VM phase for various exchange and correlation potentials and experiment (Refs. 8–10).

		Expt.	GGA+U				LDA	GGA
	U_{eff} (eV)		5	6	7	8		
$Fe^{2.5+}$	B_{dip}		−3.00	−2.98	−2.95	−2.87	−2.13	−2.83
	B_{orb}		−3.11	−2.99	−2.84	−2.74	−5.47	−4.56
	B_{contact}		41.17	40.96	41.45	41.17	33.10	36.36
	B_{tot}	~30	35.06	34.98	35.67	35.56	25.50	28.98
	δ	~0.5	0.53	0.52	0.51	0.49	0.60	0.60
	eQV_{zz}	~0.1	0.12	0.13	0.13	0.13	0.19	−0.27

pound it seems that GGA+U (with U in the range of 5–8 eV) overestimates contact (and total) hyperfine fields a bit.

In order to obtain the isomer shift of a given atom one has to compare its density at the nucleus (ρ_0) with a reference, which in our case is body-centered cubic (bcc) α-Fe. For this purpose bcc Fe (with lattice constant a=2.865 Å) was calculated with the same R_{MT} of 0.95 Å using the GGA functional and 10 000 k points (which corresponds to 891 k points in the irreducible Brillouin zone) with spin-orbit coupling enabled (the GGA+U method was not used in this case because it would yield wrong results for an itinerant metal). The ρ_0 values are directly available from the calculation. The isomer shifts δ can be calculated using the following expression:

$$\delta = \alpha(\rho_0^{\text{sample}} - \rho_0^{\text{reference}}), \tag{3}$$

where α is a proportionality constant that can be estimated through calibration. In the recent DFT calculation published by Wdowik and Ruebenbauer[27] α was found to be −0.291 a.u.^{3} mm/s, which is slightly larger than the commonly used value of −0.27 from the work of Duff.[28] The isomer shifts obtained with the former value for the CO phase differ slightly from the experimental values but the difference between them (~0.6 mm/s) is in excellent agreement with experiment. For the VM phase the agreement is even better with an average δ of ~0.5 mm/s for different U_{eff} which is also the value observed in experiment. Again, GGA results would not agree with experiment for the CO phase and lead to a much smaller difference between the isomer shifts of the two Fe sites.

The electric field gradients V_{zz} can be directly calculated using *ab initio* methods,[29,30] but experimentally only the product of nuclear and electronic contributions in the form of the quadrupole coupling constant eQV_{zz} can be measured. In order to compare theory with experiment one needs a value for the nuclear quadrupole moment Q, which was determined by Dufek *et al.*[29] to be about 0.16 b (1 b=10^{-28} m^2) by comparing the theoretical and experimental data for a large number of compounds. With this value the relation between EFG and quadrupole splitting is approximately $\text{EFG}[10^{21}\ \text{V/m}^2] \approx 3eQV_{zz}[\text{mm/s}]$.[30]

The calculated EFGs of both modifications are in good agreement with the known experimental data. Also in this case the LDA or GGA predictions are significantly different from experiment in the CO case. Unfortunately we were not able to get experimental data for the yttrium compound but—based on the existing data for Sm, Tb, and Gd analogs—we are able to conclude that the results do not change significantly when the rare-earth ion is altered.

E. Magnetic structure

For the investigated structures several magnetic arrangements are possible depending on the size of the chosen supercell. Therefore we concentrated our efforts first on checking whether the long-range magnetic order found in experiment agrees with the most stable theoretical structure. For this purpose we calculated and compared the total energies of several different magnetic arrangements for the CO phase using the $1\times2\times1$ supercell described above. For the VM phase we verified that the experimentally observed magnetic arrangement with a direct FM coupling through the yttrium layer has a lower total energy than the type-G AFM arrangement, which is the ground state of the CO phase. For the latter calculations we used a $2\times2\times2$ supercell. In order to allow for different magnetically ordered states, we lowered the symmetry of the supercells by splitting the equivalent iron sites into 8 (CO) and 16 (VM) independent positions (see Sec. III B for details) wherever necessary (i.e., for AFM-FM in x, types F, A, and C, and AFM-FM in yz for CO and for the G-type arrangement for the VM modification). With this splitting the space group of both structures changes to $Pmm2$. The investigated magnetic structures are listed in Table X (the + and − symbols represent the relative direction of the magnetic moments), and together with Fig. 1 all magnetic arrangements are clearly defined. The naming of the individual arrangements is either derived from the work of Wollan and Koehler[20] or chosen by describing the type of coupling in a particular plane (e.g., "AFM-FM in x" stands for an antiferromagnetic structure but with ferromagnetic coupling of the magnetic moments in the x direction). The results for the CO phase are listed in Table XI. The obtained energies strongly support the experimental findings; in the CO phase the experimentally found magnetic arrangement (AFM G type) (see Fig. 1) is the most stable one among the tested configurations and in particular the ferromagnetic phase is much less favorable.

The CO and VM phases of $YBaFe_2O_5$ differ not only in the valences of the Fe atoms but also in their long-range

TABLE X. Magnetic arrangements calculated for the CO phase. + and − depict the relative direction of the magnetic moments for the iron atoms, whose indices are given. Arrangements are ordered by their relative stability.

	Fe							
Arrangement	$1_{1\alpha}$	$1_{1\beta}$	$1_{2\alpha}$	$1_{2\beta}$	$2_{1\alpha}$	$2_{1\beta}$	$2_{2\alpha}$	$2_{2\beta}$
AFM G-type	+	+	−	−	−	−	+	+
AFM-FM in x	+	−	−	+	+	−	−	+
AFM C-type	+	−	−	+	−	+	+	−
Ferrimagnetic	+	+	+	+	−	−	−	−
AFM-FM in xz	+	+	−	−	+	+	−	−
AFM F-type	+	−	+	−	+	+	−	−
AFM A-type	+	−	+	−	+	−	+	−
AFM-FM in yz	+	−	+	−	−	+	−	+
Ferromagnetic	+	+	+	+	+	+	+	+

magnetic order. While for the CO phase the AFM G-type structure was found experimentally, for the VM modification this magnetic order is *not* the most stable structure, but the magnetic structure changes at the Verwey temperature to an AFM structure which has direct FM Fe-Fe coupling across the Y layer (see Fig. 2). We finally tested this for both modifications (using $2\times2\times2$ supercells) and found in fact that for the VM phase the experimental long-range order is more stable by about 24 meV/f.u. than the AFM G-type structure. On the other hand, for the CO phase the AFM G-type magnetic arrangement is more stable by about 8.6 meV/f.u. (see Table XI), in full agreement with experiment. It should be noted that such small energy differences were expected according to estimates from the ratio of direct exchange and superexchange for a linear Fe-Fe bond.[31] Apparently the larger d_{z^2} occupation in the VM modification leads to a dominance of the direct Fe-Fe exchange and FM coupling, which is not present in the CO phase.

1. Calculation of exchange interactions

Based on the results discussed above we calculated the exchange interactions J_{ij} between the iron atoms for the CO phase. We focused our efforts on the superexchange interactions, i.e., the interactions between neighboring iron atoms connected via an oxygen atom and used supercells with eight independent iron sites for this purpose. For an isotropic and bilinear pair of spins $\vec{S}_1$ and $\vec{S}_2$, the energy e_{12} is given by the following expression:

$$e_{12} = J(\vec{S}_1\vec{S}_2), \tag{4}$$

where J stands for the exchange integral between the spins. To calculate this integral in a complex system with many different magnetic sublattices one can use the following equation (see the work of Novak and Rusz[32] for a thorough derivation):

$$J_{ij} = \frac{\Delta_{ij} - \Delta_i - \Delta_j}{S_i S_j n_i z_{ij} \sigma_i^{(0)} \sigma_j^{(0)}}. \tag{5}$$

Note, that this expression is only valid for systems showing collinear magnetism (which is true for the CO phase). The Δ_i variables correspond to the change in total energy per f.u. when the spin on sublattice i is inverted, while Δ_{ij} refers

TABLE XI. Energy differences per f.u. (meV) of different magnetic arrangements with respect to the most stable AFM G-type structure of the CO phase. ΔE^{DFT} from direct DFT calculations (column 2), $\Delta E^{J_{\mathrm{calc}}}$ using the calculated J values from Table XII (column 4) and $\Delta E^{J_{\mathrm{lsf}}}$ from J values obtained by least-squares fit (column 5). Contributions of J values in column 3.

Arrangement	ΔE^{DFT}	Contribution	$\Delta E^{J_{\mathrm{calc}}}$	$\Delta E^{J_{\mathrm{lsf}}}$
AFM G-type (expt.)	0		0	0
AFM-FM in x	36.7	J^a_{23}	41.4	44.7
AFM C-type	46.7	J^c_{23}	55.9	52.4
Ferrimagnetic	69.6	$\frac{J^b_{33}+J^b_{22}}{2}$	79.1	81.1
AFM-FM in xz	89.9	$J^a_{23}+J^c_{23}$	97.3	97.1
AFM F-type	107.1	$\frac{J^a_{23}+J^c_{23}+J^b_{33}}{2}$	110.8	107.1
AFM A-type	124.4	$J^a_{23}+\frac{J^b_{22}+J^b_{33}}{2}$	120.5	125.8
AFM-FM in yz	129.8	$J^c_{23}+\frac{J^b_{22}+J^b_{33}}{2}$	135.0	133.5
Ferromagnetic	194.9	$J^a_{23}+J^c_{23}+\frac{J^b_{22}+J^b_{33}}{2}$	176.4	178.1
CO phase with VM arrangement	8.6			

TABLE XII. Calculated exchange interactions J using Eq. (5) (column 6) and by the least-squares fit to the energies in Table XI (column 7, together with the estimated error). Experimental values (Ref. 31) in column 8. Difference energies Δ per f.u. and exchange parameters J in meV.

Interaction	Iron atoms	Δ_i	Δ_j	Δ_{ij}	Theory [Eq. (5)]	Theory (least-squares fit)	Expt.
J^b_{33}	$Fe1^{3+}_{1\alpha}$-$Fe1^{3+}_{2\alpha}$	53.3	53.3	44.5	10.0	9.4(2.0)	5.9
J^b_{22}	$Fe2^{2+}_{1\alpha}$-$Fe2^{2+}_{2\alpha}$	29.5	29.5	42.0	4.3	5.7(3.3)	3.4
J^a_{23}	$Fe1^{3+}_{1\alpha}$-$Fe2^{2+}_{1\alpha}$	53.3	29.5	62.1	4.2	4.5(0.7)	
J^c_{23}	$Fe1^{3+}_{1\alpha}$-$Fe1^{2+}_{1\beta}$	53.3	29.8	54.8	5.6	5.2(0.7)	6.0[a]

[a]Experimentally averaged as $J_{23}=\frac{2J^a_{23}+J^c_{23}}{3}$.

to a spin flip on two sublattices i and j. The σ_i are the relative directions of the spins (i.e., ± 1) S_i, where S_i is $\frac{5}{2}$ for Fe^{3+} and 2 for Fe^{2+}. n_i is the number of atoms belonging to the sublattice i of the unit cell (n is 1 for all eight iron sites in our case). z_{ij} stands for the number of sites of sublattice j that are neighbors of the site from sublattice i. Also this value is 1 for all iron sites in our case.

We calculated the energy difference Δ_i for the inversion of a single divalent and trivalent iron site (the energy difference should be the same on all isovalent sites due to symmetry) as well as for spin arrangements where the spins of *two* of the independent iron sites are inverted (this corresponds to the Δ_{ij} values). With these energies one is able to calculate the exchange interaction between the different iron atoms. Based on these considerations there are *four* different superexchange interactions in the case of the CO phase: $J^b_{22}(Fe2^{2+}_{1\alpha}$-$Fe2^{2+}_{2\alpha})$, $J^b_{33}(Fe1^{3+}_{1\alpha}$-$Fe1^{3+}_{2\alpha})$, $J^c_{23}(Fe1^{3+}_{1\alpha}$-$Fe2^{2+}_{1\beta})$, and $J^a_{23}(Fe1^{3+}_{1\alpha}$-$Fe2^{2+}_{1\alpha})$. To label the individual interactions we followed the naming scheme used in the recently published paper by Chang *et al.*[31] where the interactions were measured by inelastic neutron scattering. For each interaction J^x_{nm} the subscripts n and m denote the valences of the two interacting iron sites, whereas the superscript x describes the orientation of the interaction.

In order to verify that the four J values mentioned above describe the main magnetic interactions in this system (so that additional exchange interactions can be neglected), we used the calculated energy differences from Table XI (column 3) to obtain another set of J values with a least-squares fit approach. This was done with the contributions (each J value multiplied by S_iS_j) defined in column 3 of the same table. The resulting values were divided by 2 to avoid double counting.

In Table XII the results for J with both calculations are shown as well as the experimental values taken from the aforementioned paper.[31] We note that the two theoretical sets of J are very similar, indicating the internal numerical consistency of the calculations. Therefore additional longer-ranged exchange interactions, although existent, must be small.

All calculated J values are positive, indicating AFM coupling in each case. From a comparison with the experimental values, which were derived by fitting the inelastic neutron-scattering data, we find the correct order and magnitude for J^a_{23} and J^c_{23}, while the exchange parameters J^b_{33} and J^b_{22} between two isovalent Fe ions are a bit too large. Of course J depends on U_{eff}. We have always chosen $U_{\text{eff}}=7$ eV in all calculations but did not vary U_{eff} since such calculations are fairly expensive.

We recalculated the energy differences for the magnetic arrangements listed in Table XI using both sets of theoretical J values. The contributions of the individual J values are listed in the table in column 3. Each J value has to be multiplied by $2S_iS_j$ to obtain the given energy difference (columns 4 and 5) resulting from the exchange interactions. The resulting values are in good agreement with the energy differences obtained by DFT calculations. This proves that those four J values which describe the main superexchange interactions are really the dominant factors describing the magnetic interactions in this system, although more long-range interactions may also play some small role.

V. CONCLUSION

Understanding the Verwey transition in magnetite is still one of the hot topics in solid-state research. A big problem is the remaining uncertainty about the exact structure of magnetite below the Verwey temperature. The present work covers a much simpler model system—double-cell perovskite $YBaFe_2O_5$—to investigate the effects of the Verwey transition on various properties using DFT-based methods. This system is also a good benchmark for the power of the DFT method itself as it shows both the strengths and weaknesses of theory. Using conventional and well-established functionals such as LDA or GGA, one is not able to reproduce the experimentally found properties such as correct magnetic moments or the appearance of insulating charge order for the CO phase. Only by going beyond those schemes and using a method that can adequately describe strongly correlated systems can one be able to obtain reasonable results. In our case this was done via the GGA+U method, with which it was possible to simulate both the low-temperature CO and the high-temperature VM phase with good accuracy as the results for magnetic moments, the amount of charge ordering (obtained with AIM), and the comparison with Mössbauer experiments prove. We could also verify that the orbital ordering is the main reason for the orthorhombic distortion in the low-temperature CO phase. The occupation of the d_{xz} orbital of divalent iron is the driving force; it is doubly occupied, a distribution which leads to an orbital ordering, a charge-ordering arrangement which violates the Anderson criterion and a cooperative Jahn-Teller distortion of the whole structure due to a strong electron-lattice coupling. Overall these results for the CO phase are in agreement with

recent DFT calculations on the same compound published by Hao *et al.*[11] For the VM phase the Fe ion carries a formal valence of 5.5 based on stoichiometry, which we could verify by looking at the partial charges. In addition we found that only the d_{z^2} orbital has an occupation significantly larger than 1 and thus represents the top of the valence band. It proved to be very important to optimize the internal parameters of the structures in order to achieve accurate results, especially for the VM modification where the difference between optimized and experimental parameters is large. The appearance of a distortion in the z direction had a positive effect on the quality of the calculated EFG and isomer shifts. The magnetic moments are in good agreement with the experimental values extrapolated to 0 K. Estimating U_{eff} showed values which were in agreement with our expectations for this type of compound and with the empirical approach done before by total-energy calculations. We were also able to verify the magnetic structures found by NPD measurements for the two phases. For the CO phase we also calculated the exchange interactions between the Fe atoms along all possible superexchange paths and obtained semiquantitative agreement with experiment, but the calculated exchange coupling between two isovalent Fe ions seems to be a bit larger than in experiment.

Note added in proof. Recently, we found a paper by Vidya *et al.*[33] which presents calculations for $YBaM_2O_5$ (M = Mn, Fe, Co).

ACKNOWLEDGMENTS

The authors want to thank Pavel Karen (University of Oslo) for the experiments which were the foundation for the calculations done in this paper. Furthermore he has proven to be a source of valuable comments and interesting discussions.

[1] M. Robin and P. Day, Adv. Inorg. Chem. Radiochem. **10**, 247 (1968).
[2] E. Verwey, Nature (London) **144**, 327 (1939).
[3] F. Walz, J. Phys.: Condens. Matter **14**, R285 (2002).
[4] P. Hohenberg and W. Kohn, Phys. Rev. **136**, B864 (1964).
[5] W. Kohn and L. J. Sham, Phys. Rev. **140**, A1133 (1965).
[6] P. Blaha, K. Schwarz, G. K. H. Madsen, D. Kvasnicka, and J. Luitz, WIEN2K, an augmented plane wave+local orbitals program for calculating crystal properties, Techn. Universität Wien, Getreidemarkt 9/156 A, 1060 Wien, Austria, 2001.
[7] P. Woodward and P. Karen, Inorg. Chem. **42**, 1121 (2003).
[8] J. Lindén, P. Karen, A. Kjekshus, J. Miettinen, T. Pietari, and M. Karppinen, Phys. Rev. B **60**, 15251 (1999).
[9] P. Karen, P. M. Woodward, J. Lindén, T. Vogt, A. Studer, and P. Fischer, Phys. Rev. B **64**, 214405 (2001).
[10] J. Lindén, P. Karen, H. Yamauchi, and M. Karppinen, Hyperfine Interact. **156-157**, 321 (2004).
[11] X. Hao, Y. Xu, M. Lv, D. Zhou, Z. Wu, and J. Meng, Inorg. Chem. **47**, 4734 (2008).
[12] K. Schwarz and P. Blaha, Comput. Mater. Sci. **28**, 259 (2003).
[13] J. P. Perdew and Y. Wang, Phys. Rev. B **45**, 13244 (1992).
[14] J. P. Perdew, K. Burke, and M. Ernzerhof, Phys. Rev. Lett. **77**, 3865 (1996).
[15] V. I. Anisimov, J. Zaanen, and O. K. Andersen, Phys. Rev. B **44**, 943 (1991).
[16] V. I. Anisimov and O. Gunnarsson, Phys. Rev. B **43**, 7570 (1991).
[17] G. K. H. Madsen and P. Novák, Europhys. Lett. **69**, 777 (2005).
[18] P. W. Anderson, Phys. Rev. **102**, 1008 (1956).
[19] J. B. Goodenough, Phys. Rev. **100**, 564 (1955).
[20] E. O. Wollan and W. C. Koehler, Phys. Rev. **100**, 545 (1955).
[21] M. J. Ruiz-Aragón, E. Morán, U. Amador, J. L. Martínez, N. H. Andersen, and H. Ehrenberg, Phys. Rev. B **58**, 6291 (1998).
[22] J. Lindén, P. Karen, J. Nakamura, M. Karppinen, and H. Yamauchi, Phys. Rev. B **73**, 064415 (2006).
[23] E. Goering, S. Gold, M. Lafkioti, and G. Schütz, Europhys. Lett. **73**, 97 (2006).
[24] D. J. Huang, C. F. Chang, H.-T. Jeng, G. Y. Guo, H.-J. Lin, W. B. Wu, H. C. Ku, A. Fujimori, Y. Takahashi, and C. T. Chen, Phys. Rev. Lett. **93**, 077204 (2004).
[25] R. Bader, *Atoms in Molecules: A Quantum Theory* (Oxford University Press, New York, 1994).
[26] A. Kokalj, J. Mol. Graphics Modell. **17**, 176 (1999).
[27] U. D. Wdowik and K. Ruebenbauer, Phys. Rev. B **76**, 155118 (2007).
[28] K. J. Duff, Phys. Rev. B **9**, 66 (1974).
[29] P. Dufek, P. Blaha, and K. Schwarz, Phys. Rev. Lett. **75**, 3545 (1995).
[30] H. M. Petrilli, P. E. Blöchl, P. Blaha, and K. Schwarz, Phys. Rev. B **57**, 14690 (1998).
[31] S. Chang, P. Karen, M. P. Hehlen, F. R. Trouw, and R. J. McQueeney, Phys. Rev. Lett. **99**, 037202 (2007).
[32] P. Novak and J. Rusz, Phys. Rev. B **71**, 184433 (2005).
[33] R. Vidya, P. Ravindran, K. Knizek, A. Kjekshus, and H. Fjellvag, Inorg. Chem. **47**, 6608 (2008).